Volume 3
Number 1
7 January 2022
Pages 1–690

Materials Advances

rsc.li/materials-advances

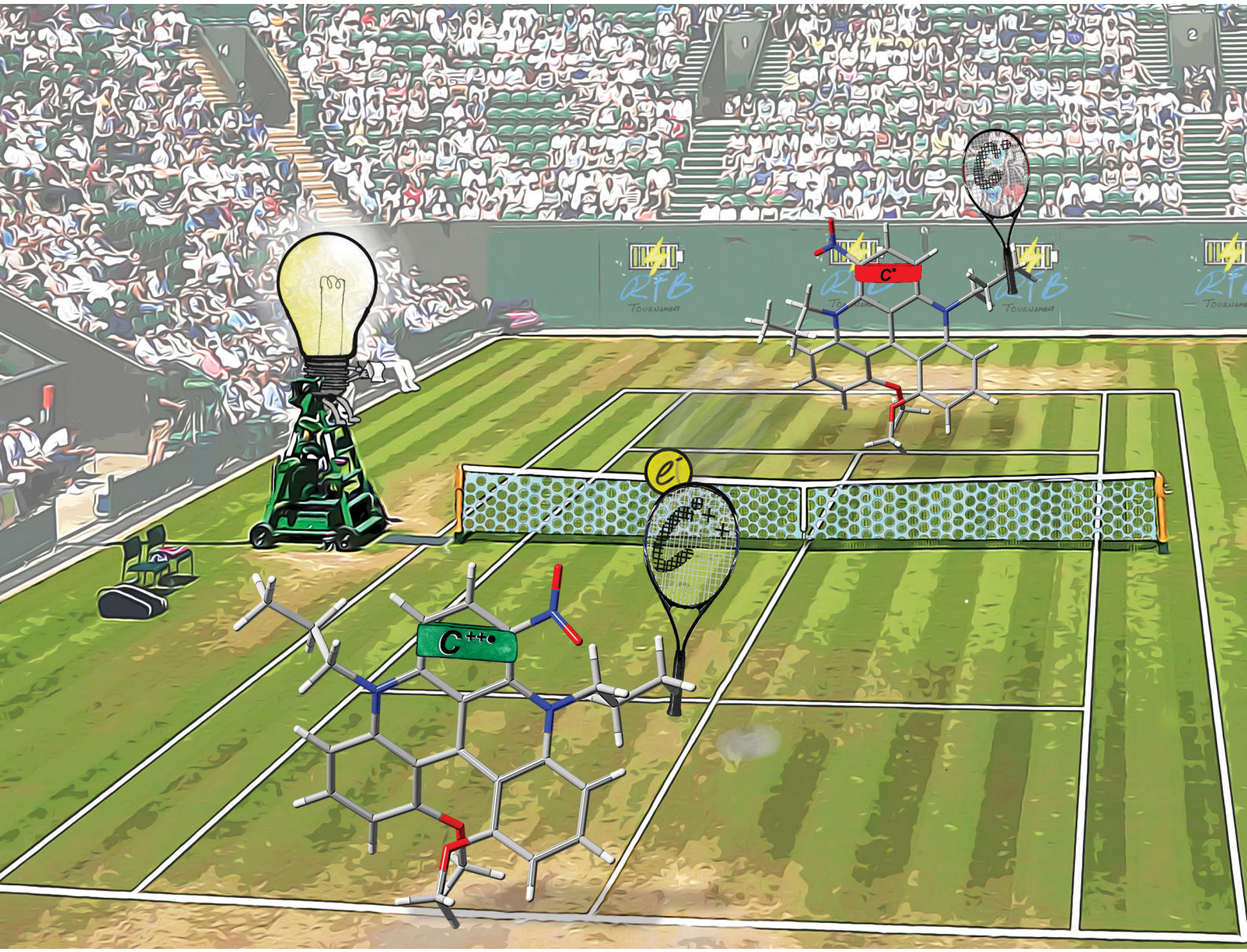

ISSN 2633-5409

ROYAL SOCIETY OF CHEMISTRY

PAPER

Thomas L. Gianetti *et al.*
Increased performance of an all-organic redox flow battery model *via* nitration of the [4]helicenium DMQA ion electrolyte

Materials Advances

ROYAL SOCIETY OF CHEMISTRY

PAPER

View Article Online
View Journal | View Issue

Cite this: *Mater. Adv.*, 2022, 3, 216

Increased performance of an all-organic redox flow battery model *via* nitration of the [4]helicenium DMQA ion electrolyte†

Jules Moutet, David Mills, Md Mubarak Hossain and Thomas L. Gianetti *

Redox flow batteries (RFBs), through their scalable design and virtually unlimited capacity, are promising candidates for large-scale energy storage. While recent advances in the development of redox-active bipolar organic molecules satisfy the prerequisites for the pioneering emergence of symmetrical all-organic redox flow batteries (SORFBs), problems of low durability or low energy density remain a bottleneck for their wide-spread application. The present work reports that nitration of the [4]helicenium dimethoxyquinacridinium ($DMQA^+$) ion core ($^{NO2}C^+$) results in a significantly enhanced electrochemical performance of $DMQA^+$ as the electrolyte for SORFBs. The physical and kinetic properties of $^{NO2}C^+$ were evaluated by cyclic voltammetry (CV) and UV-visible spectroscopy in acetonitrile and compared to those of its precursor ($^{H}C^+$). The ability for electron storage of $^{NO2}C^+$ was investigated in three different types of static H-cell experiments. In the first experiment, $^{NO2}C^+$ provided an open circuit voltage (OCV) of 2.24 V resulting in demonstrated good stability, as well as high coulombic (>98%) efficiencies, over more than 200 charge/discharge cycles. In the second experiment, a charge–discharge cycling over the entire redox window of $^{NO2}C^+$ (OCV > 3 V) resulted in 80 cycles at a potential energy density above 12 W h L^{-1}. During the last experiment, a bipolarization stress-test was performed in which $^{NO2}C^+$ demonstrated a remarkable durability of 90 cycles at 100% load with a perfect retention of capacity and coulombic efficiency. The enhanced electrochemical performance of this redox material highlights that $DMQA^+$ ions are robust and versatile materials for the emergence of SORFBs.

Received 1st October 2021,
Accepted 9th November 2021

DOI: 10.1039/d1ma00914a

rsc.li/materials-advances

Introduction

Despite the increased need for renewable energy, the intermittent availability of these energy sources prevents them from meeting the essential requirement of a constant supply.[1] Incorporation of efficient storage systems, such as batteries, is a growing need for optimal integration of renewable energies into the grid.[2–4] Currently, the most widespread electric energy storage systems (EESs) are mainly based on high-performance lithium-ion batteries.[5,6] However, the availability of this metal is quickly being overtaken by the current demand.[7,8] One promising technology to be incorporated as an EES is that of redox flow batteries (RFBs).[9–13] RFBs store energy in liquid electrolytes that contain dissolved redox-active species, which are pumped from storage tanks to an electrochemical cell. The conversion between electrical and chemical energies occurs at the cell, resulting in a decoupled power and capacity. As a consequence, their capacity is virtually unlimited since it relies on the volume of the electrolyte stored in the tanks, which makes RFBs suitable for large-scale electricity storage.[14] Currently, aqueous all-vanadium-based RFBs (VRFBs), which use water-soluble vanadium ions in different oxidation states as redox-active species, are considered a robust choice and are an established EES technology.[10,15–17] VRFBs are also an outstanding example of a symmetrical RFB using only one element in both electrolytes, allowing the crossing of electrolytes to result only in self-discharge of the battery and not in persistent cross-contamination.[18] Although other metal-based electrolytes have been explored,[19–22] the use of metal-based RFBs is limited due to their high cost and toxicity.[23,24] Driven by the continuous demand for low-cost and large-scale organic RFBs (ORFBs), redox-active organic materials (ROMs) have emerged as attractive and powerful systems thanks to their sustainable, synthetically tunable, and potentially inexpensive raw materials.[25–32]

To be competitive with existing VRFBs, special attention must be paid to the ORFB energy density (E_d). This is defined as $E_d = nFV_{cell}C_{active}0.5$ (E_d in W h L^{-1})[26] where n is the number of electrons in the redox process, F is the Faraday constant in A h L^{-1}, V_{cell} is the open circuit voltage, and C_{active} is the concentration of redox-active species (equal to the equivalent

University of Arizona, Department of Chemistry and Biochemistry, Tucson, AZ, USA. E-mail: tgianetti@arizona.edu

† Electronic supplementary information (ESI) available. See DOI: 10.1039/d1ma00914a

electron concentration at the cathode and the anode). Evidently, with the aim of increasing the energy density of ORFBs, three parameters must be addressed:

The solubility of the ROM, which is already commonly adjustable in aqueous media,[29,33,34] but is still rarely optimized for non-aqueous solvents.[35,36]

The open circuit voltage (OCV), which in the case of a symmetrical RFB, corresponds to a potential gap between the redox species.

The number of electrons involved and/or the number of redox processes of the ROM.

While impressive advances have been made in recent years in the field of aqueous RFBs,[37–39] the overall ROM performance is inherently limited by the narrow electrochemical window of water (<1.23 V). Therefore, research for providing high energy density ORFB systems has already started to move towards non-aqueous (NA) systems based on organic solvents, with wider electrochemical stability window to develop the so called NAORFBs.[40–49]

We have recently demonstrated that 1,3-dipropylodimethoxy-quinolinoacridinium tetrafluoroborate salt helicene (denoted $^{H}C^{+}$, see Scheme 1)[41] possess remarkable performance as an electrolyte material in symmetrical ORFBs *via* its three stable $^{H}C^{\bullet+}/^{H}C^{+}/^{H}C^{\bullet}$ redox states. The $^{H}C^{+}$ ions showed impressive redox stability, and a high OCV of 2.12 V in a static RFB model.[50] Here, we investigate the study and use of a derivative of this $DMQA^{+}$ after introducing an electron withdrawing group as an electrolyte for high-voltage RFBs. Access to a nitro-derivative was easily achieved by the post-synthetic nitration of $^{H}C^{+}$ under acidic conditions in dichloromethane (Scheme 1).[51] This nitro-helicenium ion [^{n}Pr-DMQA^{NO2}][BF_4], denoted as $^{NO2}C^{+}$ throughout this report, is expected to fulfill the three points mentioned above to increase the energy density. Herein, we report the in-depth study of the electronic behaviors of $^{NO2}C^{+}$ as an improved ROM for NAORFBs.

Experimental

Chemicals, reagents, and synthesis of $^{NO2}C^{+}$

All solvents were purified by a solvent purification system (SPS) or distilled over the drying agents indicated. Dried solvents and liquid reagents were transferred by oven-dried syringes or hypodermic syringes. The supporting electrolyte tetrabutyl-ammonium hexafluorophosphate ($TBAPF_6$) was recrystallized three times from ethanol, then dried at 80 °C under vacuum for three days prior to use. The racemic mixture of 1,13-dimethoxy-6-nitro-5,9-dipropyl-9,13*b*-dihydro-5*H*-quinolino[2,3,4-*kl*]acridinium tetrafluoroborate salt ($^{NO2}C^{+}$) was prepared according to Lacour *et al.*'s report and was purified by crystallization *via* slow vapor diffusion of Et_2O in concentrated DCM or CH_3CN solutions.[51]

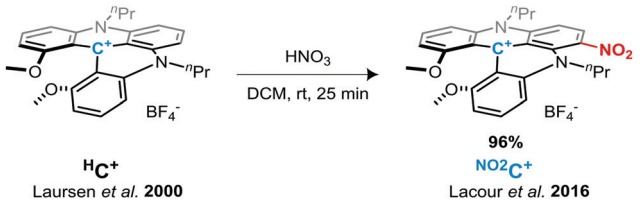

$^{H}C^{+}$ Laursen *et al.* **2000**

$^{NO2}C^{+}$ Lacour *et al.* **2016**

Scheme 1 Nitration of *N,N′*-dialkyl-1,13-dimethoxyquinacridinium ($DMQA^{+}$) $^{H}C^{+}$ to form $^{NO2}C^{+}$.

UV-vis measurements

Absorption spectra were recorded on a ThermoScientific Evolution 220 UV-Visible spectrophotometer at 25 °C in dried CH_3CN at different concentrations. All recorded samples were prepared in a Vigor glovebox under an inert N_2 atmosphere with H_2O/O_2 concentrations maintained below 1 ppm. A 3 mL gas-tight cuvette (Quartz Cuvette Self Masking Screw Cap) was used for anaerobic acquisition of all spectra.

Electrochemical studies

Electrochemical analyses were conducted inside a N_2-filled MBraun glovebox using a BioLogic SP-200 potentiostat/galvanostat and the EC-Lab® software (v11.33) from BioLogic Science Instruments. For convenience, all potentials are given *versus* the internal reference electrode $AgNO_3$/Ag.

Cyclic voltammograms (CV) were measured in a three-electrode electrochemical cell, consisting of a platinum wire counter electrode, a $AgNO_3$/Ag reference electrode (0.01 M $AgNO_3$ in 0.1 M $TBAPF_6$ in CH_3CN), and a platinum working electrode (0.031 cm^2, CH Instrument, Inc.). The working electrode was polished prior to each recording using aluminium oxide in polishing paper and anhydrous CH_3CN to remove residual particles. CVs were recorded at different scan rates (10, 25, 75, 100, 250, 400, and 500 mV s^{-1}) in an CH_3CN electrolyte containing 1 mM $^{NO2}C^{+}$ and 0.1 M $TBAPF_6$.

Static cell experiments

Galvanostatic cycling experiments under static conditions were carried out in a custom-made glass H-cell (see Fig. S12, ESI†) with a classical three electrode system within a silver reference electrode (0.01 M $AgNO_3$/Ag in 0.1 M $TBAPF_6$ in CH_3CN). A 2 mm fine porous glass frit (4–5.5 μm hole diameter) was used as the separator[43,44] and 10 mL of $^{NO2}C^{+}$ solution (0.1 M $TBAPF_6$) was used to study the cycling in the cell. Reticulated vitreous carbon (RVC) electrodes (100 ppi Duocel®) were cut into rods of the dimensions 0.5 cm × 0.5 cm × 4 cm and positioned about 2 cm deep in solution (active surface ~ 33 cm^2 per electrode). To rule out contamination processes, the electrodes were singly used. A constant current followed by a constant voltage galvanostatic charging (CCCV GCPL protocol) at |5| mA current was applied *via* RVC electrodes. During charge–discharge experiments the compartments of both cells were continuously stirred at 1000 rpm.

Results and discussion

Electrochemical studies

During this work, acetonitrile was chosen as the model solvent, since it provides an exceptionally wide electrochemical window

(~6.0 V), has a positive impact on energy density,[40,46] and has proved to be suitable with $DMQA^+$.[50]

Cyclic voltammetry experiments in acetonitrile (0.1 M $TBAPF_6$) showed three single-electron redox events for $^{NO2}C^+$ (Fig. 1a, b solid black line and Fig. S1, ESI†), contrasting with the two redox events of its parent $^{H}C^+$ (Fig. 1b, dotted grey line). In its initial oxidation state, $^{NO2}C^+$ forms a pair with a BF_4^- anion (Fig. 1a blue frame). Differential voltammetry (DPV) experiments (Fig. 1b transparent colored plot, and Fig. S2, ESI†) were performed to accurately obtain the half-wave potential of the redox processes ($E_{1/2}$) observed. The single-electron oxidation event observed at $E_{1/2}^{Ox}$ = 1.35 V, corresponds to the formation of the dication radical $^{NO2}C^{\bullet++}$ whose two charges are then compensated by the BF_4^- and PF_6^- anions present in solution. The potential of this redox couple $^{NO2}C^{\bullet++}/^{NO2}C^+$ appears 310 mV higher than the one obtained for $^{H}C^+$ ($E_{1/2}^{Ox}$ = 0.98 V) due to the electron withdrawing group NO_2. Upon scanning to the anodic region of potential, the one-electron reduction of this nitro-[4]helicenium leads to the formation of the neutral radical $^{NO2}C^{\bullet}$ at potential $E_{1/2}^{Red1}$ = −0.89 V. The $^{NO2}C^{\bullet}/^{NO2}C^+$ redox event occurs at a potential shifted by +250 mV compared to the event observed with $^{H}C^+$ ($E_{1/2}^{Red}$ = −1.14 V). Finally, a second reversible mono-electronic event in reduction occurs at $E_{1/2}^{Red2}$ = −1.67 V. This latter is attributed to the redox pair $^{NO2}C^{\bullet}/^{NO2}C^{\bullet\bullet-}$ corresponding to the formation of the biradical anionic state $^{NO2}C^{\bullet\bullet-}$, whose charge will be compensated by the presence of TBA^+ in solution.[51,52]

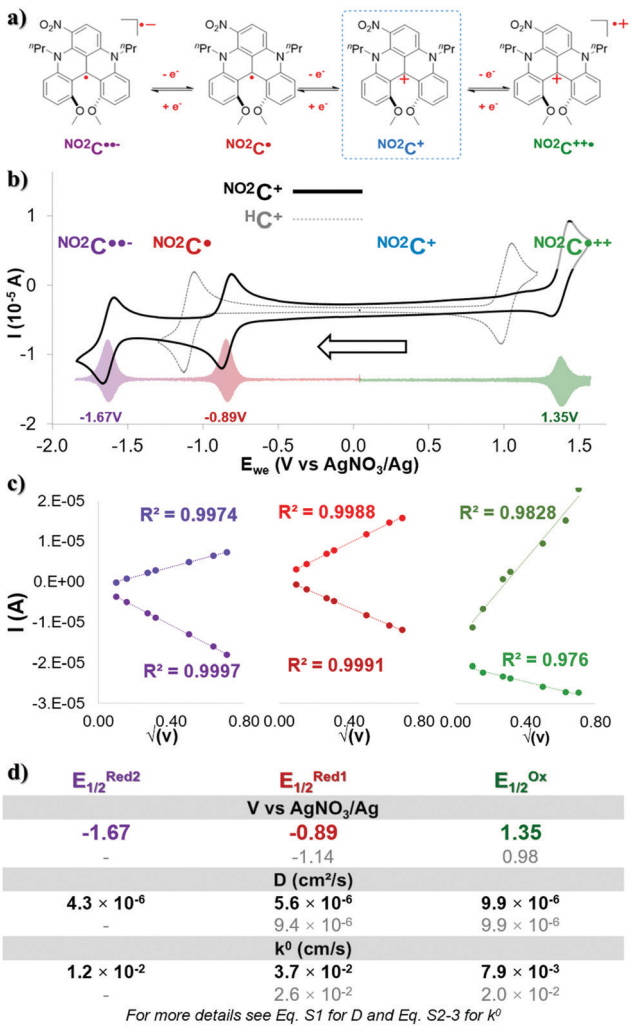

Fig. 1 (a) Four different oxidation states of $^{NO2}C^+$. Counter-anions and counter-cations have been removed for clarity. (b) CV at scan rate of 100 mV s^{-1} for $^{NO2}C^+$ in black, $^{H}C^+$ in grey and (c) measured intensity (I) reported as a function of the square root of the scan rate (10–500 mV s^{-1}) for the 3 electronic processes of 1.0 mM $^{NO2}C^+$ solution in 0.1 M $TBAPF_6$/CH_3CN. (d) D and k^0 determined by studying CVs at different scan rates from 10 to 500 mV s^{-1} for $^{NO2}C^+$ in black, $^{H}C^+$ in grey.

The reversibility of these electronic processes has been investigated through the acquisition of CV at different scan rates in a three-electrode cell (see Fig. S3, ESI†). The exhibited linear relation between measured intensity (I) and the square root of the scan rate (Fig. 1c and Fig. S4, ESI†) indicates that the electrolyte is freely diffusing, and a complete reversibility of the three electronic processes is maintained at each scan rate. The essential electrochemical kinetic parameters were extracted from these plots (Fig. 1d). The Randles–Sevcik equation application (eqn S1), gave access to an experimental diffusion coefficient (D) value of 9.9 × 10^{-6} cm^2 s^{-1} for the $^{NO2}C^{\bullet++}/^{NO2}C^+$ pair. It is an identical value to the one exhibited by $^{H}C^+$ (Fig. 1d in grey $D(E^1{}_{1/2Ox})$ = 9.9 × 10^{-6} cm^2 s^{-1}) and slightly higher than the value for a recent catholyte for ORFB application.[34,36,43,47,48] On the other hand the values for the reductive processes for $^{NO2}C^+/^{NO2}C^{\bullet}$ (D = 5.6 × 10^{-6} cm^2 s^{-1}) and $^{NO2}C^{\bullet}/^{NO2}C^{\bullet\bullet-}$ (D = 4.3 × 10^{-6} cm^2 s^{-1}) couples are approximately twice as low overall as the value for the $^{H}C^+$ reduction process ($D(E^1{}_{1/2Red})$ = 9.4 × 10^{-6} cm^2 s^{-1}) and are similar to the values for recent anolytes studied.[36,41,42,47,53,54]

The useful work reported by Lavagnini *et al.* was used to determine the electron transfer rate constant (k^0) using these D-values (Fig. 1d and eqn S2, S3, ESI†).[55,56] The values of k^0 = 3.7 × 10^{-2} cm s^{-1} for $^{NO2}C^+/^{NO2}C^{\bullet}$ and k^0 = 1.2 × 10^{-2} cm s^{-1} for $^{NO2}C^{\bullet}/^{NO2}C^{\bullet\bullet-}$ redox couples are quite similar, and their average provides a value close to that of the couple $^{H}C^+/^{H}C^{\bullet}$ (k^0 = 2.6 × 10^{-2} cm s^{-1}). However, the k^0 = 7.9 × 10^{-3} cm s^{-1} value of $^{NO2}C^{\bullet++}/^{NO2}C^+$ is lower than that observed for $^{H}C^+$ (k^0 = 2.0 × 10^{-2} cm s^{-1}) and lower than that identified for the $^{NO2}C^+$ reduction phenomena which are both comparable to redox shuttles used in NAORFBs.[42,43,46]

We attribute the slight differences in parameters observed between each process due to the loss of symmetry of the [4]helicenium core by the addition of the $-NO_2$ moiety. The electrokinetic parameters obtained suggest that this electrolyte is suitable for ORFB application. We could expect in a symmetrical use, an OCV of 2.24 V. The presence of a second process in reduction, accessible by a second mono-electronic transfer implies the possible access to two electron storage with $^{NO2}C^{\bullet\bullet-}$ formation, with a high OCV of 3.02 V.

Saturation concentration of the different oxidation states

The saturation concentrations of $^{NO2}C^+$ and $^{NO2}C^{\bullet}$ in acetonitrile were evaluated using UV-vis spectroscopy (see Fig. S5–S8, ESI†). Despite numerous attempts to synthesize and isolate $^{NO2}C^{\bullet++}$ in

its pure form, our efforts have been unfruitful. The $^{NO2}C^{\bullet\bullet-}$ formation *via* an alkaline double-reduction (KC_8) has been also investigated. Crystals were formed at low temperature (−35 °C) but were highly unstable upon increasing temperatures and insufficiently stable to be used for obtaining a UV-Vis calibration curve or further analysis, even with pre-cooled CH_3CN solubilization. This observation is supported by the DFT calculations (Tables S5, S6 and Fig. S9–S11, ESI†), indicating a predominance of the more reactive triplet state for $^{NO2}C^{\bullet\bullet-}$ (see Fig. S11, ESI†). In pure CH_3CN, $^{NO2}C^{+}_{sat}$ exhibits a saturation concentration of 154 mM, whereas that for $^{NO2}C^{\bullet}_{sat}$ is slightly lower with a value of 110 mM. In both states, the solubility exhibited is above >0.1 M. The introduction of a nitro group modifies the electrochemical behavior of the DMQA scaffold, and also significantly increases its solubility ($^{H}C^{+}_{sat}$ = 32 mM *vs.* $^{NO2}C^{+}_{sat}$ = 154 mM in acetonitrile). This increased solubility will lead to a higher energy density of $E_d(^{NO2}C^{+})$ = 9.25 W h L^{-1} compared to that of $E_d(^{H}C^{+})$ = 1.84 W h L^{-1}. In a single late-functionalization step, the energy density of the previous ROM was increased by a factor of 5.

Galvanostatic cycling with potential limitation cycling

The electrochemical stability of the electrolyte $^{NO2}C^{+}$ was evaluated by bulk electrolysis charge/discharge cycling using a three-electrode H-cell as model for a redox flow cell setup. Although it does not allow working at high concentrations, Hansmann *et al.* have shown that such electrochemical cell designs are acceptable test beds for organic ROMs in RFB performance.[42,44]

Mono-polarization cycling, OCV = 2.24 V

We first investigated the use of this $^{NO2}C^{+}$ as an electrolyte for ORFB application in a symmetrical step. Both sides of the cell were equally filled with a 1.0 mM solution of $^{NO2}C^{+}$ (0.1 M $TBAPF_6/CH_3CN$) (Fig. 2a). One cycle corresponds to a charge followed by a discharge. During the charge, in the "catholyte" compartment (the E_w side of the cell) $^{NO2}C^{+}$ is oxidized to $^{NO2}C^{\bullet++}$, while in the "anolyte" compartment (E_c of the cell) $^{NO2}C^{+}$ is reduced to $^{NO2}C^{\bullet}$.

In the first instance, mono-electronic transfer at 90% of theoretical capacity (90% state of charge, "SOC") cycles (Fig. 2 and Fig. S13, S14, ESI†) were performed. A constant current followed by a constant voltage galvanostatic charging (CCCV GCPL protocol) of |5| mA was applied with potential boundaries at −1.49 V and −0.49 V *vs.* E_{ref}. During the charge–discharge cycles two plateaux at *ca.* −0.92 V and −0.86 V in the E_w voltage curves were observed and assigned to the electronic processes of the $^{NO2}C^{+}/^{NO2}C^{\bullet}$ redox couple (Fig. 2b and Fig. S15, ESI†). Satisfactorily, the cell monitoring (Fig. 2c) shows that the Coulombic efficiency (CE, green triangle) remains constant and close to 100% throughout the experiment. Furthermore, the capacity Q (red and blue squares) exhibited a plateau, with an initial capacity (90% SOC or $Q_{theoretical}$) retention over ~200 cycles. The decrease in the capacity started at the 186th cycle, and the system then lost 0.32% capacity retention per cycle, reaching a value of Q = 50% $Q_{theoretical}$ at the 340th cycle. The cycling was stopped at the 400th cycle and

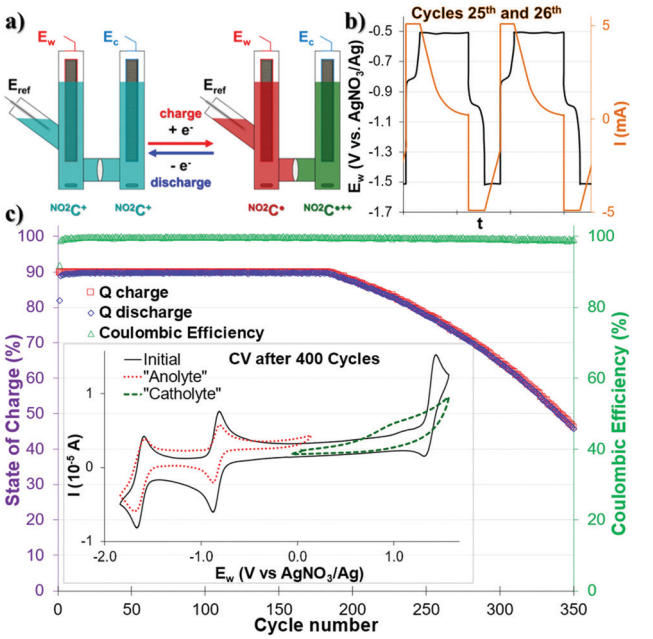

Fig. 2 (a) Scheme showing the mono-electronic charge–discharge cycles in a symmetric H-cell. The color code is indicative of the electrolyte oxidation degree. (b) Zoom-in of E_{we} during the 25th and 26th cycles of cycling and species formation in the E_{ref} compartment. (c) Q of charge–discharge processes and Coulombic efficiency monitoring over 350 cycles of mono-electronic exchange. Inset shows CV analysis at 100 mV s^{-1} of the respective contents of each side of the cell after 400 cycles.

the final capacity reached was Q_{final} = 33% $Q_{theoretical}$. Differences in solution mobility and speed of electronic exchange led to faster system fatigue and electrolyte deterioration.

The CV analysis of each compartment after 400 monopolarization cycles of the H-cell revealed that the catholytic compartment is strongly degraded with a broadened and poorly defined profile, highlighting a deterioration of the oxidation process of $^{NO2}C^{+}$ into $^{NO2}C^{\bullet++}$ (Fig. 2c). In the anolytic compartment, we noted a beginning of fatigue after 400 cycles (see Fig. S15, ESI†) with the $E^{Red1}_{1/2}$ process of $^{NO2}C^{+}$ to $^{NO2}C^{\bullet}$ decreased slightly in intensity and resolution. Thus, although the introduction of a NO_2 group seems to have a negative effect on the robustness of our electrolyte, this comes along with a dramatic increase in the solubility of this ROM. In a symmetrical cell with monopolarization it allowed increasing the gap between the two redox events in oxidation and reduction, resulting in a theoretical E_d = 9.25 W h L^{-1}, much higher than the 1.84 W h L^{-1} of its parent ion $^{H}C^{+50}$ that can be delivered for almost 200 cycles. It has also been noted that, the monopolarization cycles seemed to not affect the second electronic transfer $E^{Red2}_{1/2}$ at −1.67 V which led us to expect a resilient behaviour during 2-electron reduction storage experiments.

Double reduction cycling, OCV = 3.02 V

The use of multi-electron storage in order to increase the energy density of a system is currently being studied for ARFBs,[35,45,57,58] but remains underexplored for NARFBs.[34,36]

Since $^{NO2}C^{+}$ is able to store two electrons, *via* two one-electron processes in the anodic potential (first the $^{NO2}C^{\bullet}$ state, then the $^{NO2}C^{\bullet\bullet-}$ state) we studied the viability of a two-electron storage ORFB through a H-cell. In this configuration, the cell is loaded asymmetrically with the same ROM on both sides: on the catholyte side the $^{NO2}C^{+}$ concentration is twice as high as that on the anolyte side (ratio 2 : 1, for the same 0.1 M $TBAPF_6$ supporting salt) (Fig. 3a). In this way, the following battery will be able to store twice as much current, accessing a high voltage of 3.02 V, without cross-contamination risk and increasing the amount of ROM needed by only half. If we consider C_{max} $^{NO2}C^{+}$ = 154 mM with OCV of 3.02 V, a maximum value of E_d = 12.47 W h L^{-1} could be calculated for this double reduction cycling test, *i.e.* 6.8 times more energy stored than in the unsubstituted helicenium $^{H}C^{+}$.[50]

Before any test, the anolyte side was checked *via* CV to verify the reversibility of the two processes $E_{1/2}^{Red1}$ and $E_{1/2}^{Red2}$ in the initial state. The concentration of the anolyte compartment – half of that of the catholyte compartment – is distinguishable by a current intensity twice as low as that of the catholyte solution used (Fig. 3b inset purple trace).

A CCCV GCPL protocol of |5| mA with potential boundaries at −2.07 V and −0.49 V *vs.* E_{ref} limited at 90% SOC was then applied and monitored over 125 cycles (Fig. 3b). It was noted that despite an excellent CE close to 100%, the capacity of our system fluctuated a lot over the course of the experiment. Thus, as early as the 6th cycle, it was noted that the capacity of our system decreased from 90% to 70% in cycle 10. We observe a "rebound" between cycles 10 and 20, leading to the capacity of our system being <70% $Q_{theoretical}$. The capacity of our system slightly increases then to reach a value of 84% in cycle 74, and then quickly drops. It then loses 0.75% per capacity cycle, reaching a value of 53% in the 125th cycle. This type of behavior also observed by Binnemans' group for a double reduction of their ROM, has not yet been elucidated.[36] Unfortunately, no clearly defined plateau in the E_w voltage curves was observed during the charge–discharge cycles (see Fig. S17, ESI†). The intensity of the current used and the low ROM concentration of the monitored compartment are probably to blame (0.5 mM at |5| mA).

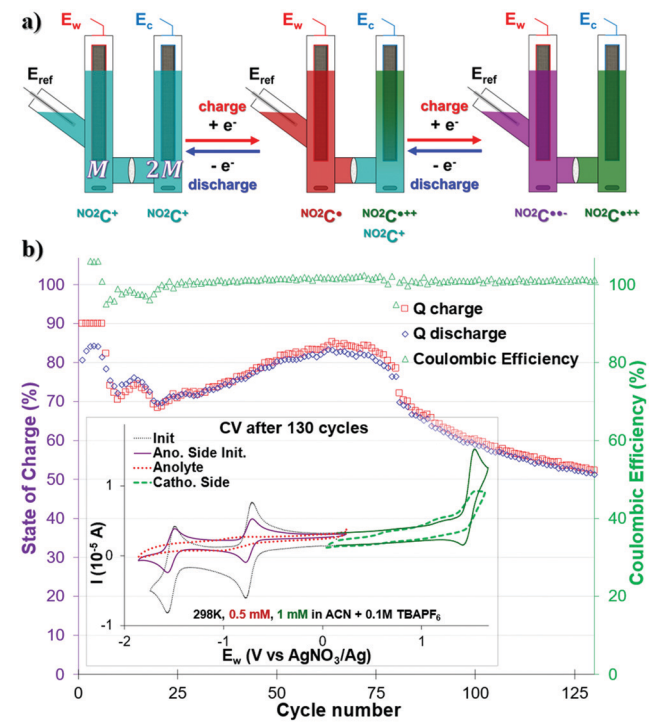

Fig. 3 (a) Scheme showing the bi-electronic reduction charge–discharge cycles in a 1 : 2 $^{NO2}C^{+}$ concentration H-cell. The color code is indicative of the electrolyte oxidation degree. (b) *Q* of charge–discharge processes and Coulombic efficiency monitoring over 130 cycles of bi-electronic exchange. Inset shows CV analysis at 100 mV s^{-1} of the respective contents of each side of the cell after 130 cycles.

The CV analysis of each compartment after 130 bi-reduction cycles of the H-cell (Fig. 3b inset and Fig. S17, ESI†) provided further information. As noted for the monopolarization experiment, the catholytic compartment consisting of the $^{NO2}C^{+}$ into $^{NO2}C^{\bullet+}$ process degraded and exhibited a broadened profile (Fig. 3b inset green trace). The anodic compartment, which was stable during the monopolarization experiment, shows a serious deterioration of the electro-active material after 130 cycles (Fig. 3b inset red trace). The electronic processes $E_{1/2}^{Red1}$ and $E_{1/2}^{Red2}$ are almost indistinguishable, and the electrochemical profile is severely altered, more than the cathodic compartment.

In view of these results, one can conclude that the low stability of $^{NO2}C^{\bullet\bullet-}$, previously noted and supported by DFT calculations (see Fig. S9–S11, ESI†), is one of the weak points of the system. Furthermore, the appearance of a "bounce" in the capacity between cycle 10 and 20 could be linked to diffusion effects. Indeed, our H-cell model is a so-called "static" model, and in the configuration where $^{NO2}C^{+}$ is present in a 1 : 2 ratio, diffusion effects at the interface, which is here a porous frit and not a selective membrane, may have a major role. Nevertheless, while the robustness of the system needs to be improved, the simple addition of an NO_2 group onto the DMQA core allowed access to a second process in reduction, and a very high voltage battery of 3.02 V.

Bipolarization cycling, "stress-test"

The symmetrical properties of $^{NO2}C^{+}$, where the system can be charged independently by transferring electrons into one or the other side of the cell, allow us to carry out bi-electronic cycling tests by polarizing the battery in the opposite direction. Given the poor results obtained in the process of $E_{1/2}^{Red2}$, we did not consider it necessary to carry out this experiment with $^{NO2}C^{\bullet\bullet-}$ species as anolyte. This protocol consists of a highly stressful two-electron charge and discharge process on each side of the cell at 100% SOC. This means that the species $^{NO2}C^{\bullet+}$ and $^{NO2}C^{\bullet}$ will be formed successively in each compartment over time (Fig. 4a). These two-electron cycling processes, labeled "Stress Test" are likely to shorten the life of the battery and are not meant to describe the energy storage ability of our electrolyte under these conditions.[44] The experiment will however provide information about the sturdiness of this electrolyte.

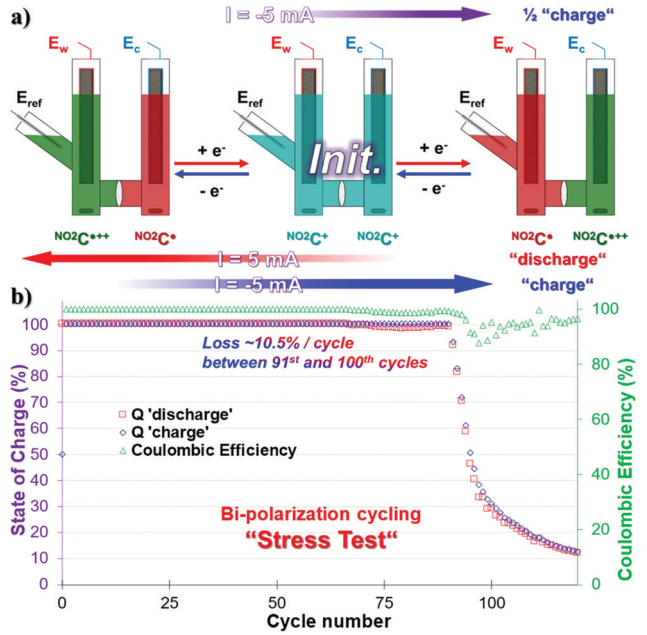

Fig. 4 (a) Scheme showing the bi-electronic charge–discharge cycles in a symmetric H-cell as stress test. The color code is indicative of the electrolyte oxidation degree. (b) Q of charge–discharge processes and Coulombic efficiency monitoring over 120 cycles of bi-electronic exchange.

A CCCV GCPL sequence with a |5| mA current, setting potential boundaries at 1.55 V and −1.49 V *vs.* E_{ref}, was therefore started from the initial state of this symmetrical battery (Fig. 4a). In the first step, the working electrode side of the cell was "charged" with electrons with a cutoff potential of −1.49 V for full reduction of $^{NO2}\mathbf{C}^{+}$ to $^{NO2}\mathbf{C}^{\bullet}$ (Fig. 4a, purple arrow). Then a positive 5 mA current was applied at 1.55 V (Fig. 4a, red arrow) and two electrons were sequentially exchanged, taking $^{NO2}\mathbf{C}^{\bullet}$ to $^{NO2}\mathbf{C}^{\bullet+}$. Finally, the current was reversed to −1.49 V to "charge" the electrons in the working electrode side of the cell back to $^{NO2}\mathbf{C}^{\bullet}$ (Fig. 4a, blue arrow). The continuous alternation of red and blue steps corresponds to a cycle. Unfortunately, over the course of the experiment, monitoring the value of E_w voltage curves is not representative of the conversion processes of $^{NO2}\mathbf{C}^{\bullet}$ to $^{NO2}\mathbf{C}^{+}$ and $^{NO2}\mathbf{C}^{+}$ to $^{NO2}\mathbf{C}^{\bullet+}$ (see Fig. S20 and S21, ESI†).

As shown by the green triangles, the CE was constant and close to 100% until the 90th cycle, with a quasi-constant full capacity Q = 100% SOC for two-electron cycling. Then a drastic drop in Q with an irrecoverable capacity loss of 70% capacity between the 91st and 100th cycles was observed, and the system then degraded more slowly to reach a value of 12.5% SOC in the 120th cycle (Fig. 4b). This was associated with a slight decrease in CE starting at the 91st cycle which varies between 90% and 98% until the end of the experiment. This electrolyte fatigue has been correlated to the degradation of the species during the oxidation phenomenon in $^{NO2}\mathbf{C}^{\bullet+}$ and is probably the source of weakness of our battery.

However, during the stress test the $^{NO2}\mathbf{C}^{+}$ demonstrated a higher robustness than its parent $^{H}\mathbf{C}^{+}$. Indeed, 90 cycles could be reached without degradation of the capacity, *i.e.* +12.5% compared to $^{H}\mathbf{C}^{+}$.[50] We can directly correlate this robustness improvement to the increase in the solubility of $^{NO2}\mathbf{C}^{+}$ and more specifically to the increase in solubility of the radical dication $^{NO2}\mathbf{C}^{\bullet++}$ compared to $^{H}\mathbf{C}^{\bullet++}$ which allows a longer cyclability over time under extremely stressful conditions.

Conclusions

The need to evolve RFBs tends towards the use of organic bipolar redox-active molecules to promote a more robust and reliable design.[49] This is an elegant solution to the challenge of cross-contamination and membrane costs. In the case of NARFB, the choice of the solvent will allow a very large potential window and increase the accessible energy density. The question of ROM solubility remains a critical point. During this study, we set out to improve these different parameters. Thus, by a quasi-quantitative late nitration of our previous ROM, we were able to:

boost the solubility of our $\mathbf{C}^{+}$ electrolyte by 4.8 times allowing a longer lifetime during the stress test,

expand the open circuit voltage (OCV) between $E_{1/2}^{Ox}$ and $E_{1/2}^{Red1}$ by 120 mV (monopolarization),

increase the number of reversible electronic events to three, with a second event, allowing an OCV $E_{1/2}^{Ox} - E_{1/2}^{Red2}$ of 3.02 V (double reduction cycling).

Thus, despite the moderate stability of $^{NO2}\mathbf{C}^{++\bullet}$ and $^{NO2}\mathbf{C}^{-\bullet\bullet}$, this simple modification of the $DMQA^{+}$ core allowed us to multiply the initial energy density by 5 times in the case of monoelectronic cycling. Moreover, the double anode reduction cycling demonstrated an E_d value of 12.5 W h L^{-1} that is closer to the one offered by current aqueous VRFBs (15–25 W h L^{-1}).[59]

The simplicity of the structural modification and the results obtained underline the value that the DMQA core presents as a ROM library for symmetrical ORFBs.

Author contributions

T. L. G. and J. M. wrote the manuscript, planned the experiments, and discussed their conclusions. J. M. conducted all experiments; D. M. performed the DFT calculations; M. M. H. synthesized $^{NO2}\mathbf{C}^{+}$.

Conflicts of interest

There are no conflicts to declare.

Acknowledgements

We are grateful to the University of Arizona, the Research Corporation for Science Advancement, Cottrell Scholarship 2021, and the Salt River Project for financially supporting this work.

References

1 M. S. Dresselhaus and I. L. Thomas, *Nature*, 2001, **414**, 332–337.
2 Z. Yang, J. Zhang, M. C. W. Kintner-Meyer, X. Lu, D. Choi, J. P. Lemmon and J. Liu, *Chem. Rev.*, 2011, **111**, 3577–3613.
3 S. P. S. Badwal, S. S. Giddey, C. Munnings, A. I. Bhatt and A. F. Hollenkamp, *Front. Chem.*, 2014, **2**, 1–28.
4 T. M. Gür, *Energy Environ. Sci.*, 2018, **11**, 2696–2767.
5 J. B. Goodenough, M. S. Whittingham and A. Yoshino, *Rep. - Swed. Acad. Eng. Sci. Finl.*, 2019, 1.
6 A. Masias, J. Marcicki and W. A. Paxton, *ACS Energy Lett.*, 2021, 621–630.
7 J.-M. Tarascon and M. Armand, *Nature*, 2001, **414**, 359–367.
8 M. Winter, B. Barnett and K. Xu, *Chem. Rev.*, 2018, **118**, 11433–11456.
9 J. Rugolo and M. J. Aziz, *Energy Environ. Sci.*, 2012, **5**, 7151–7160.
10 G. L. Soloveichik, *Chem. Rev.*, 2015, **115**, 11533–11558.
11 M. Park, J. Ryu, W. Wang and J. Cho, *Nat. Rev. Mater.*, 2017, **2**, 16080.
12 L. F. Arenas, C. Ponce de León and F. C. Walsh, *Curr. Opin. Electrochem.*, 2019, **16**, 117–126.
13 D. G. Kwabi, Y. Ji and M. J. Aziz, *Chem. Rev.*, 2020, **120**, 6467–6489.
14 P. Alotto, M. Guarnieri and F. Moro, *Renewable Sustainable Energy Rev.*, 2014, **29**, 325–335.
15 W. Lu, X. Li and H. Zhang, *Phys. Chem. Chem. Phys.*, 2017, **20**, 23–35.
16 H. R. Jiang, W. Shyy, M. C. Wu, R. H. Zhang and T. S. Zhao, *Appl. Energy*, 2019, **233–234**, 105–113.
17 H. R. Jiang, J. Sun, L. Wei, M. C. Wu, W. Shyy and T. S. Zhao, *Energy Storage Mater.*, 2020, **24**, 529–540.
18 R. A. Potash, J. R. McKone, S. Conte and H. D. Abruña, *J. Electrochem. Soc.*, 2016, **163**, A338–A344.
19 W. Wang, S. Kim, B. Chen, Z. Nie, J. Zhang, G.-G. Xia, L. Li and Z. Yang, *Energy Environ. Sci.*, 2011, **4**, 4068–4073.
20 P. J. Cabrera, X. Yang, J. A. Suttil, K. L. Hawthorne, R. E. M. Brooner, M. S. Sanford and L. T. Thompson, *J. Phys. Chem. C*, 2015, **119**, 15882–15889.
21 Y. A. Gandomi, D. S. Aaron, J. R. Houser, M. C. Daugherty, J. T. Clement, A. M. Pezeshki, T. Y. Ertugrul, D. P. Moseley and M. M. Mench, *J. Electrochem. Soc.*, 2018, **165**, A970–A1010.
22 M. Park, E. S. Beh, E. M. Fell, Y. Jing, E. F. Kerr, D. Porcellinis, M. Goulet, J. Ryu, A. A. Wong, R. G. Gordon, J. Cho and M. J. Aziz, *Adv. Energy Mater.*, 2019, **9**, 1900694.
23 *DOE Office of ARPR-E. ARPA-E, GRIDS Program Overview*, https://arpa-e.energy.gov/sites/default/files/documents/files/GRIDS_ProgramOverview.pdf.
24 *U.S. DEPARTMENT OF HEALTH AND HUMAN SERVICES Public Health Service Agency for Toxic Substances and Disease Registry*, ATSDR's Toxicological Profiles, CRC Press, 2012.
25 T. B. Schon, B. T. McAllister, P.-F. Li and D. S. Seferos, *Chem. Soc. Rev.*, 2016, **45**, 6345–6404.
26 J. Winsberg, T. Hagemann, T. Janoschka, M. D. Hager and U. S. Schubert, *Angew. Chem., Int. Ed.*, 2017, **56**, 686–711.
27 X. Wei, W. Pan, W. Duan, A. Hollas, Z. Yang, B. Li, Z. Nie, J. Liu, D. Reed, W. Wang and V. Sprenkle, *ACS Energy Lett.*, 2017, **2**, 2187–2204.
28 T. Janoschka, C. Friebe, M. D. Hager, N. Martin and U. S. Schubert, *ChemistryOpen*, 2017, **6**, 216–220.
29 Y. Ding, C. Zhang, L. Zhang, Y. Zhou and G. Yu, *Chem. Soc. Rev.*, 2018, **47**, 69–103.
30 R. F. Service, *Science*, 2018, **362**, 508–509.
31 J. Luo, B. Hu, M. Hu, Y. Zhao and T. L. Liu, *ACS Energy Lett.*, 2019, **4**, 2220–2240.
32 R. P. Fornari and P. de Silva, *Wiley Interdiscip. Rev.: Comput. Mol. Sci.*, 2020, 1–16.
33 S. Jin, Y. Jing, D. G. Kwabi, Y. Ji, L. Tong, D. De Porcellinis, M.-A. Goulet, D. A. Pollack, R. G. Gordon and M. J. Aziz, *ACS Energy Lett.*, 2019, **4**, 1342–1348.
34 J. Chai, A. Lashgari, Z. Cao, C. K. Williams, X. Wang, J. Dong and J. Jimmy Jiang, *ACS Appl. Mater. Interfaces*, 2020, **12**, 15262–15270.
35 H. Chen, Z. Niu, J. Ye, C. Zhang, X. Zhang and Y. Zhao, *ACS Appl. Energy Mater.*, 2021, **4**, 855–861.
36 P. Geysens, Y. Li, I. Vankelecom, J. Fransaer and K. Binnemans, *ACS Sustainable Chem. Eng.*, 2020, **8**, 3832–3843.
37 K. Lin, R. Gómez-Bombarelli, E. S. Beh, L. Tong, Q. Chen, A. Valle, A. Aspuru-Guzik, M. J. Aziz and R. G. Gordon, *Nat. Energy*, 2016, **1**, 16102.
38 P. Leung, T. Martin, M. Liras, A. M. Berenguer, R. Marcilla, A. Shah, L. An, M. A. Anderson and J. Palma, *Appl. Energy*, 2017, **197**, 318–326.
39 B. Hu, J. Luo, M. Hu, B. Yuan and T. L. Liu, *Angew. Chem., Int. Ed.*, 2019, **58**, 16629–16636.
40 K. Gong, Q. Fang, S. Gu, S. F. Y. Li and Y. Yan, *Energy Environ. Sci.*, 2015, **8**, 3515–3530.
41 X. Wei, W. Duan, J. Huang, L. Zhang, B. Li, D. Reed, W. Xu, V. Sprenkle and W. Wang, *ACS Energy Lett.*, 2016, **1**, 705–711.
42 K. H. Hendriks, S. G. Robinson, M. N. Braten, C. S. Sevov, B. A. Helms, M. S. Sigman, S. D. Minteer and M. S. Sanford, *ACS Cent. Sci.*, 2018, **4**, 189–196.
43 Y. Yan, S. G. Robinson, M. S. Sigman and M. S. Sanford, *J. Am. Chem. Soc.*, 2019, **141**, 15301–15306.
44 P. W. Antoni, T. Bruckhoff and M. M. Hansmann, *J. Am. Chem. Soc.*, 2019, **141**, 9701–9711.
45 L. Tong, Y. Jing, R. G. Gordon and M. J. Aziz, *ACS Appl. Energy Mater.*, 2019, **2**, 4016–4021.
46 A. Korshunov, M. J. Milner, M. Grünebaum, A. Studer, M. Winter and I. Cekic-Laskovic, *J. Mater. Chem. A*, 2020, **8**, 22280–22291.
47 X. Xing, Q. Liu, W. Xu, W. Liang, J. Liu, B. Wang and J. P. Lemmon, *ACS Appl. Energy Mater.*, 2019, **2**, 2364–2369.
48 Y. Yan, T. P. Vaid and M. S. Sanford, *J. Am. Chem. Soc.*, 2020, **142**, 17564–17571.
49 M. Li, J. Case and S. D. Minteer, *ChemElectroChem*, 2021, **8**, 1215–1232.
50 J. Moutet, J. M. Veleta and T. L. Gianetti, *ACS Appl. Energy Mater.*, 2021, **4**, 9–14.

51 I. H. Delgado, S. Pascal, A. Wallabregue, R. Duwald, C. Besnard, L. Guénée, C. Nançoz, E. Vauthey, R. C. Tovar, J. L. Lunkley, G. Muller and J. Lacour, *Chem. Sci.*, 2016, **7**, 4685–4693.
52 A. C. Shaikh, J. Moutet, J. M. Veleta, M. M. Hossain, J. Bloch, A. V. Astashkin and T. L. Gianetti, *Chem. Sci.*, 2020, **11**, 11060–11067.
53 B. Huskinson, M. P. Marshak, C. Suh, S. Er, M. R. Gerhardt, C. J. Galvin, X. Chen, A. Aspuru-Guzik, R. G. Gordon and M. J. Aziz, *Nature*, 2014, **505**, 195–198.
54 X. Yu and A. Manthiram, *Sustainable Energy Fuels*, 2018, **2**, 1452–1457.
55 R. S. Nicholson, *Anal. Chem.*, 1965, **37**, 1351–1355.
56 I. Lavagnini, R. Antiochia and F. Magno, *Electroanalysis*, 2004, **16**, 505–506.
57 C. DeBruler, B. Hu, J. Moss, X. Liu, J. Luo, Y. Sun and T. L. Liu, *Chemistry*, 2017, **3**, 961–978.
58 J. Luo, B. Hu, C. Debruler and T. L. Liu, *Angew. Chem., Int. Ed.*, 2018, **57**, 231–235.
59 A. Clemente and R. Costa-Castelló, *Energies*, 2020, **13**, 4514.